SUPPORTING INFORMATION

Tuning the 1T'/2H Phases in $W_x Mo_{1-x} Se_2$ Nanosheets

Maria S. Sokolikova,[a] Gang Cheng,[a] Mauro Och,[a] Pawel Palczynski,[a] Khalil El Hajraoui,[b,c]
Quentin M. Ramasse[b,d] and Cecilia Mattevi[*a]

[a] Department of Materials, Imperial College London, London SW7 2AZ, United Kingdom
[b] SuperSTEM Laboratory, SciTech Daresbury, Keckwick Lane, Daresbury WA4 4AD, United Kingdom.
[c] York NanoCentre & Department of Physics, University of York, York YO10 5DD, United Kingdom.
[d] School of Physics and Astronomy & School of Chemical and Process Engineering, University of Leeds, Leeds LS2 9JT, United Kingdom.

[*]corresponding author: c.mattevi@imperial.ac.uk

Supplementary Note 1. Preparation protocols.

The nominal compositions x prepared in this study, where x is the molar fraction of tungsten in the mixed transition metal precursor: [W]/([Mo]+[W]), were 1 (pristine WSe_2); 0.75; 0.50; 0.25; and 0 (pristine $MoSe_2$). The total transition metal to chalcogen ([W]+[Mo])/[Se] molar ratio was always kept at 1:4 to compensate for the Se precursor loss during the high temperature synthesis.

Table S1. Full details for the synthesis conditions used in this work. P denotes precursors taken in a powder form: solid tungsten and molybdenum hexacarbonyls and elemental selenium. SS stands for stock solution, either of tungsten or molybdenum hexacarbonyl in oleic acid, or trioctylphosphine selenide in free trioctylphosphine (TOP:Se). ν is amount (in mmol), m is mass (in mg), V is volume (in mL).

x	Material	W	ν (mmol)	m (mg) / V (mL)	Mo	ν (mmol)	m (mg) / V (mL)	Se	ν (mmol)	V (mL) / m (mg)	oleic acid V (mL)
1	WSe_2	P	0.06	20				SS	0.2	0.2	8
0.75	$W_{0.75}Mo_{0.25}Se_2$	P	0.045	15	P	0.015	3.5	SS	0.2	0.2	8
0.50	$W_{0.50}Mo_{0.50}Se_2$	P	0.03	10	P	0.03	7	SS	0.2	0.2	8
0.25	$W_{0.25}Mo_{0.75}Se_2$	P	0.015	5	P	0.045	10.5	SS	0.2	0.2	8
0	$MoSe_2$	-	-	-	P	0.06	14	SS	0.2	0.2	8
1	WSe_2	SS	0.05	*4*	-	-	-	SS	0.2	0.2	4
0.75	$W_{0.75}Mo_{0.25}Se_2$	SS	0.038	*3*	SS	0.013	*1*	SS	0.2	0.2	4
0.50	$W_{0.50}Mo_{0.50}Se_2$	SS	0.025	*2*	SS	0.025	*2*	SS	0.2	0.2	4
0.25	$W_{0.25}Mo_{0.75}Se_2$	SS	0.013	*1*	SS	0.038	*3*	SS	0.2	0.2	4
0	$MoSe_2$	-	-	-	SS	0.05	*4*	SS	0.2	0.2	4
1	WSe_2	P	0.06	20	-	-	-	P	0.2	*16*	8
0.75	$W_{0.75}Mo_{0.25}Se_2$	P	0.045	15	P	0.015	4	P	0.2	*16*	8
0.50	$W_{0.50}Mo_{0.50}Se_2$	P	0.03	10	P	0.03	7	P	0.2	*16*	8
0.25	$W_{0.25}Mo_{0.75}Se_2$	P	0.015	5	P	0.045	10.5	P	0.2	*16*	8
0	$MoSe_2$	-	-	-	P	0.06	14	P	0.2	*16*	8

Supplementary Note 2. On the reactivity of elemental selenium and phosphine selenide complex.

Elemental selenium melts at 217 °C. It reacts with various hydrocarbons (paraffins, long chain carboxylic acids and amines) releasing H_2Se [1]. Moreover, it has been reported that this reaction occurs nearly immediately in long chain alkanes at temperatures around 300 °C, when selenium is in a reactive molten form [2]. On the other hand, although it is suggested that TOP:Se decomposes in carboxylic acids, and through a series of intermediate products yields the respective carboxylic anhydride, trioctylphosphine oxide and H_2Se [3], we speculate that the rate of this reaction is slower than that with molten elemental selenium. Phosphine selenides are reported to be thermally robust, and as indirectly probed by NMR studies of the products of phosphine crossover reaction, the P=Se bond in TOP:Se is still present at temperatures up to 250 °C [4]. The slower build-up of the *in situ* formed H_2Se in the reactions with TOP:Se manifests as lower reactivity of TOP:Se precursor compared to elemental selenium.

Supplementary Note 3. On the quantitative elemental analysis using ICP AES and the estimation of active material mass loading per working electrode.

Both WSe$_2$ and MoSe$_2$ can be dissolved in strong mineral acids upon heating [5]. The analytical work with acidic solutions of tungsten and molybdenum is complicated, since in concentrated mineral acids, *e.g.* 45% HNO$_3$ required for digestion, both WSe$_2$ and MoSe$_2$ are likely to form insoluble trioxides. This could potentially lead to the loss of both tungsten and molybdenum from the analyte solutions and thus to the underestimation of transition metal concentrations. On the other hand, concentrated HNO$_3$ is likely to oxidise Se^{-2} to Se^{+4}, forming selenous acid, which is highly soluble in water. Thus, the selenium signal can be used for quantitative analysis in a wide range of concentrations.
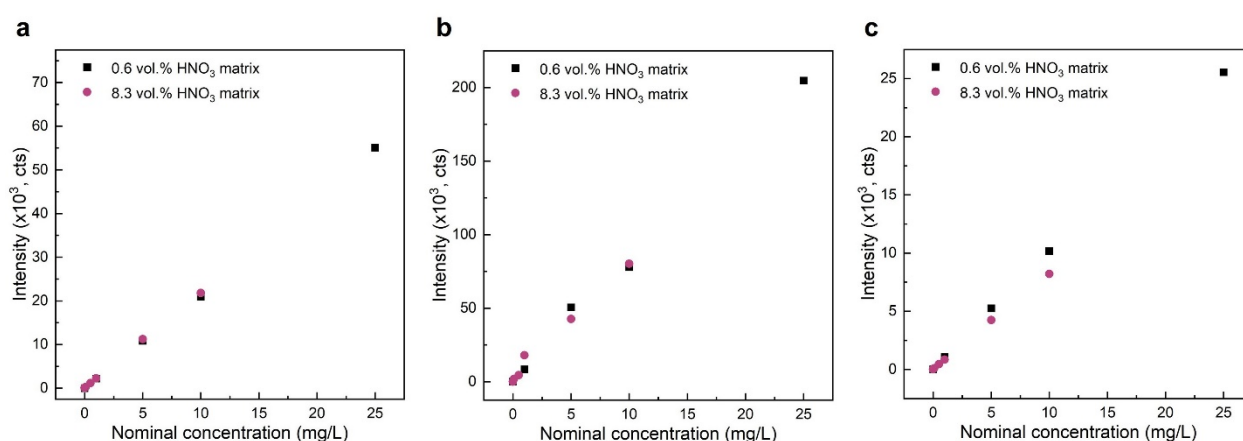
Supplementary Figure S1. Tungsten (panel a), molybdenum (panel b), and selenium (panel c) calibration curves for the ICP AES analysis acquired on the 0-25 ppm standards in two different acidic matrixes.

The digested TMD samples were diluted before the measurements, and the final concentration of HNO$_3$ ranged from 0.6 to 8.3 %. Aqueous solutions of W, Mo and Se with the known concentrations (standards) were prepared from commercial analytical reference standards for ICP and were used for calibration prior to performing the quantitative elemental analysis of binary W$_x$Mo$_{1-x}$Se$_2$ nanoflowers. We found that aqueous tungsten, molybdenum, and selenium standards were stable in the range of concentrations 0-25 ppm in these acid matrixes and showed no signs of precipitation from the analyte solutions (Figure S1).

The selenium signal was then used to estimate the amount of material v digested off CP (in μmol/cm^2) and the respective active material mass loading m per working electrode (in μg/cm^2). The reaction yield was determined as the fraction from the maximum possible amount if one assumed the transition metal precursor was fully converted into the respective diselenide.

It can be noted that in a standard synthesis (TM P + Se SS), the WSe$_2$ yield is typically higher than that of MoSe$_2$; the yields of binary W$_x$Mo$_{1-x}$Se$_2$ products fall within the range between those of the respective parent WSe$_2$ and MoSe$_2$ (Figure S2.a).

It was interesting to compare the reaction yields for both the TM P + Se SS (Figure S2.a) and the TM SS + Se SS protocols (Figure S2.b). In the case of pristine MoSe$_2$, the reaction yields appear to be very

close, regardless of the transition metal precursor type (P or SS). Whereas the concentration of tungsten stock solution was found to deviate significantly from the nominal one, which led to a considerably lower reaction yield, compared to the TM P+ Se SS, and to the tungsten deficiency in the produced binary $W_xMo_{1-x}Se_2$, as discussed in more details in the manuscript.
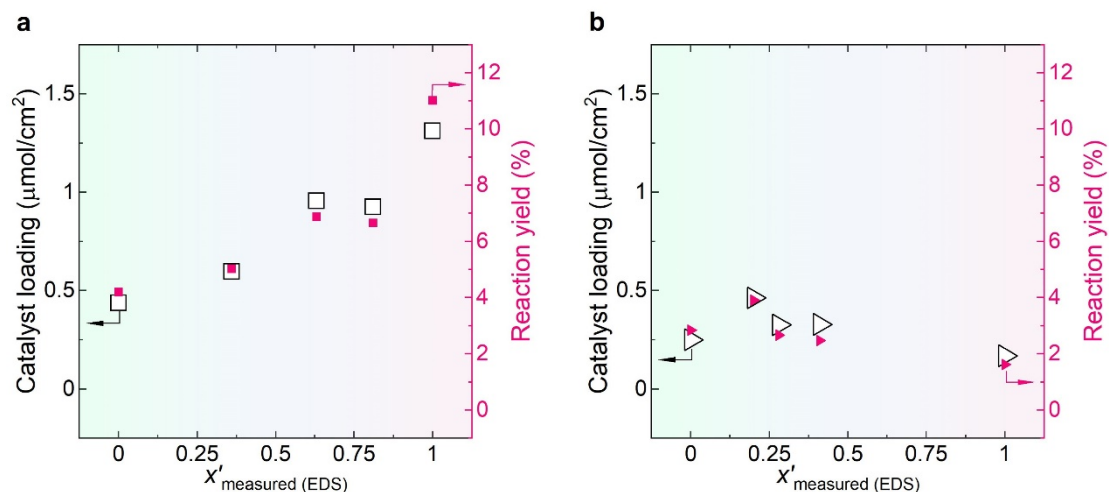

Supplementary Figure S2. Correlation between the $W_xMo_{1-x}Se_2$ catalyst mass loading per working electrode and the respective reaction yields (ICP AES) and the catalyst chemical composition x' (EDS) for the syntheses performed using mixed transition metal hexacarbonyls (TM P, panel a) and transition metal stock solutions (TM SS, panel b).
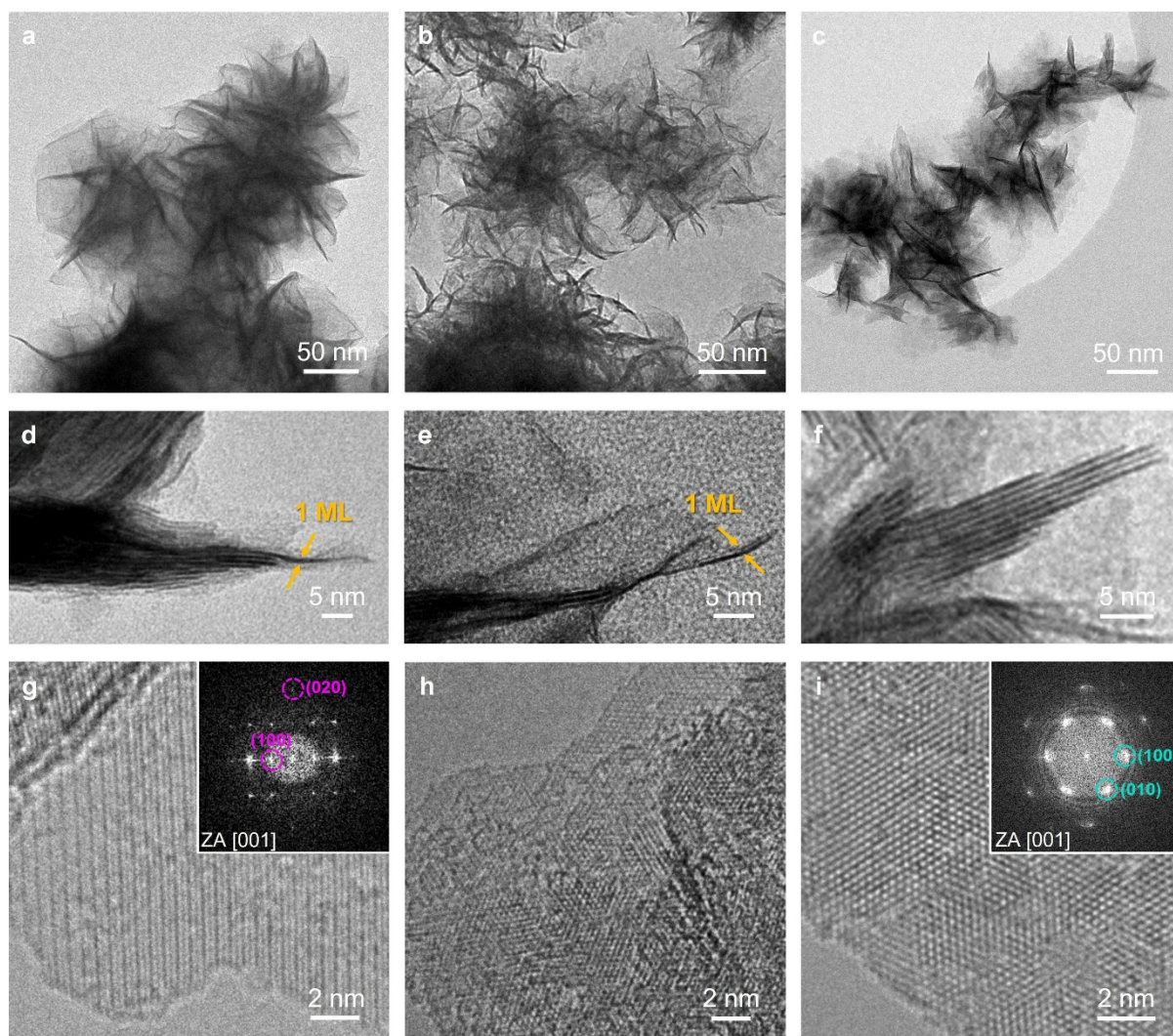
Supplementary Figure S3. Comparative morphology of $W_xMo_{1-x}Se_2$ nanoflowers and parent WSe_2 and $MoSe_2$. Low magnification TEM images of individual WSe_2 (panel a), $W_xMo_{1-x}Se_2$ $x = 0.50$ (panel b), and $MoSe_2$ (panel c) nanoflowers. Typical TEM images of the rims of individual petals of WSe_2 (panel d), $W_xMo_{1-x}Se_2$ $x = 0.50$ (panel e), and $MoSe_2$ (panel f) nanoflowers, illustrating the ultra-thin nature of WSe_2 and $W_xMo_{1-x}Se_2$ $x = 0.50$ nanostructures in contrast to the thicker petals of $MoSe_2$ nanostructures. HR TEM images of the WSe_2 (panel g), $W_xMo_{1-x}Se_2$ $x = 0.50$ (panel h), and $MoSe_2$ (panel i) nanosheets (petals) comprising the nanoflowers. The insets in panels g and i show the FFT patterns of the respective areas, clearly evidencing the 1T' (panel g) and the 2H (panel i) crystal phases.
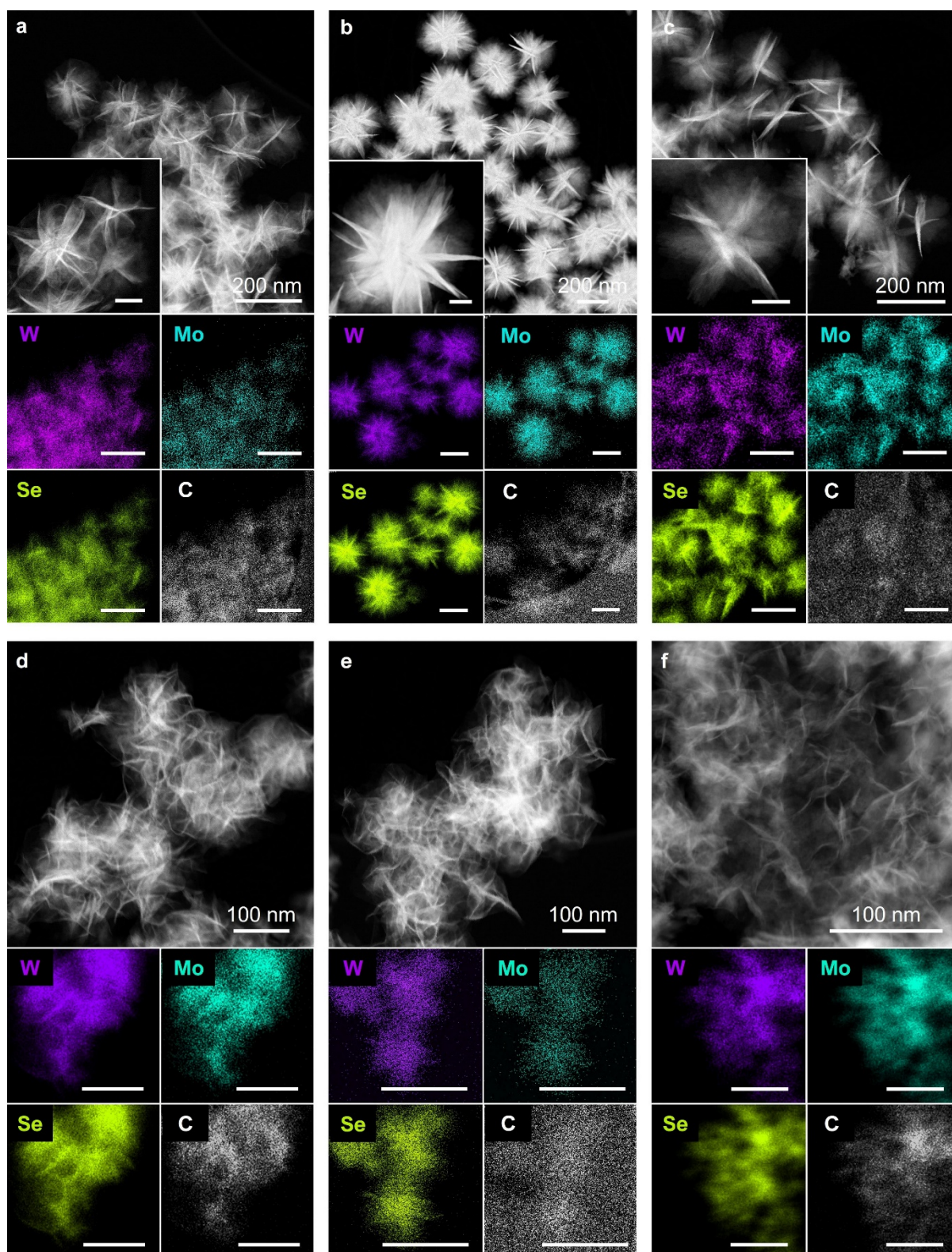
Supplementary Figure S4. The effect of selenium precursor on the morphology of $W_xMo_{1-x}Se_2$. ADF STEM images and elemental maps (W, Mo, Se, and C; scale bars 200 nm) of the ensembles of $W_xMo_{1-x}Se_2$ nanoflowers with the nominal $x = 0.75$ (panels a and d); 0.50 (panels b and e); and 0.25 (panels c and f) synthesised under the same reaction conditions, while the selenium precursor was either elemental Se (Se P, panels a-c), or fresh 1M TOP:Se complex (Se SS, panels d-f). Insets in panels a-c present the zoomed in images of individual nanoflowers; scale bars 50 nm.
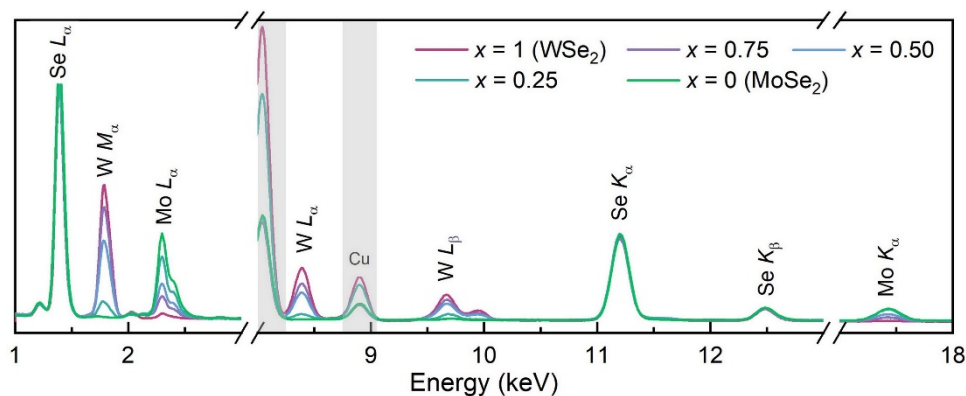
Supplementary Figure S5. Chemical composition tuning in binary $W_xMo_{1-x}Se_2$ nanoflowers. Representative STEM EDS spectra of $W_xMo_{1-x}Se_2$ nanoflowers with $x = 1$; 0.75; 0.50; 0.25; and 0. The spectra demonstrate how the chemical composition of the final $W_xMo_{1-x}Se_2$ products can be varied with the nominal x. Cu signal originates from the supporting Cu grids for TEM.
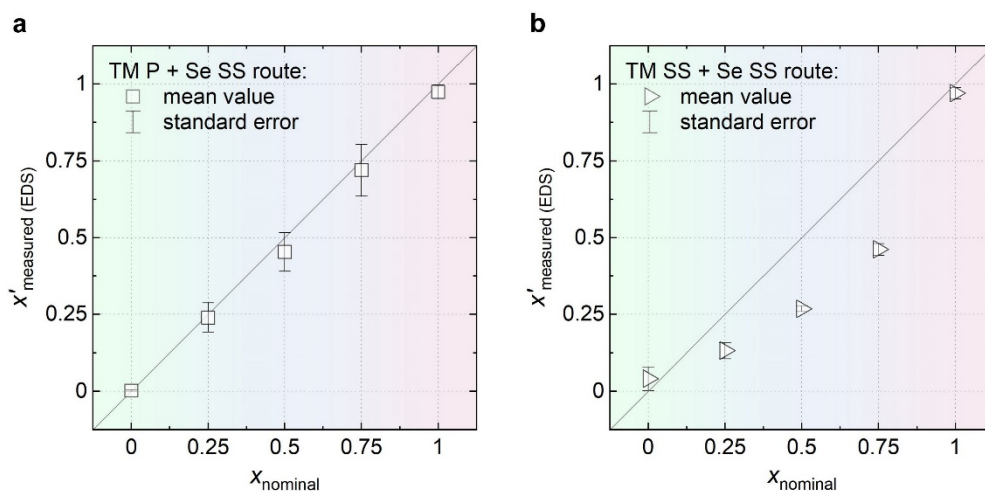
Supplementary Figure S6. The repeatability of colloidal growth procedure for $W_xMo_{1-x}Se_2$ from solid precursors (TM P, panel a) and from the respective stock solutions (TM SS, panel b). For this statistics, the synthesis of each nominal composition x was repeated 4 times from TM P + Se SS precursors and 4 times from TM SS + Se SS precursors. The open symbols represent the statistics mean values x' with their standard errors.

Table S2. The experimentally determined chemical compositions x' of batches of $W_xMo_{1-x}Se_2$ nanoflowers grown from various combinations of solid precursors (TM P and Se P) and stock solutions (TM SS and Se SS) as summarised in Figure 1.d.

| Material	$x_{nominal}$ [W]/([W]+[Mo])	$x'_{measured}$		
		TM P + Se SS	TM SS + Se SS	TM P + Se P
WSe_2	1	0.99±0.01	0.99±0.02	1
$W_{0.75}Mo_{0.25}Se_2$	0.75	0.73±0.04	0.47±0.01	0.71±0.02
$W_{0.50}Mo_{0.50}Se_2$	0.50	0.48±0.01	0.28±0.02	0.52±0.04
$W_{0.25}Mo_{0.75}Se_2$	0.25	0.24±0.03	0.14±0.02	0.08±0.01
$MoSe_2$	0	0	0.12±0.02	-
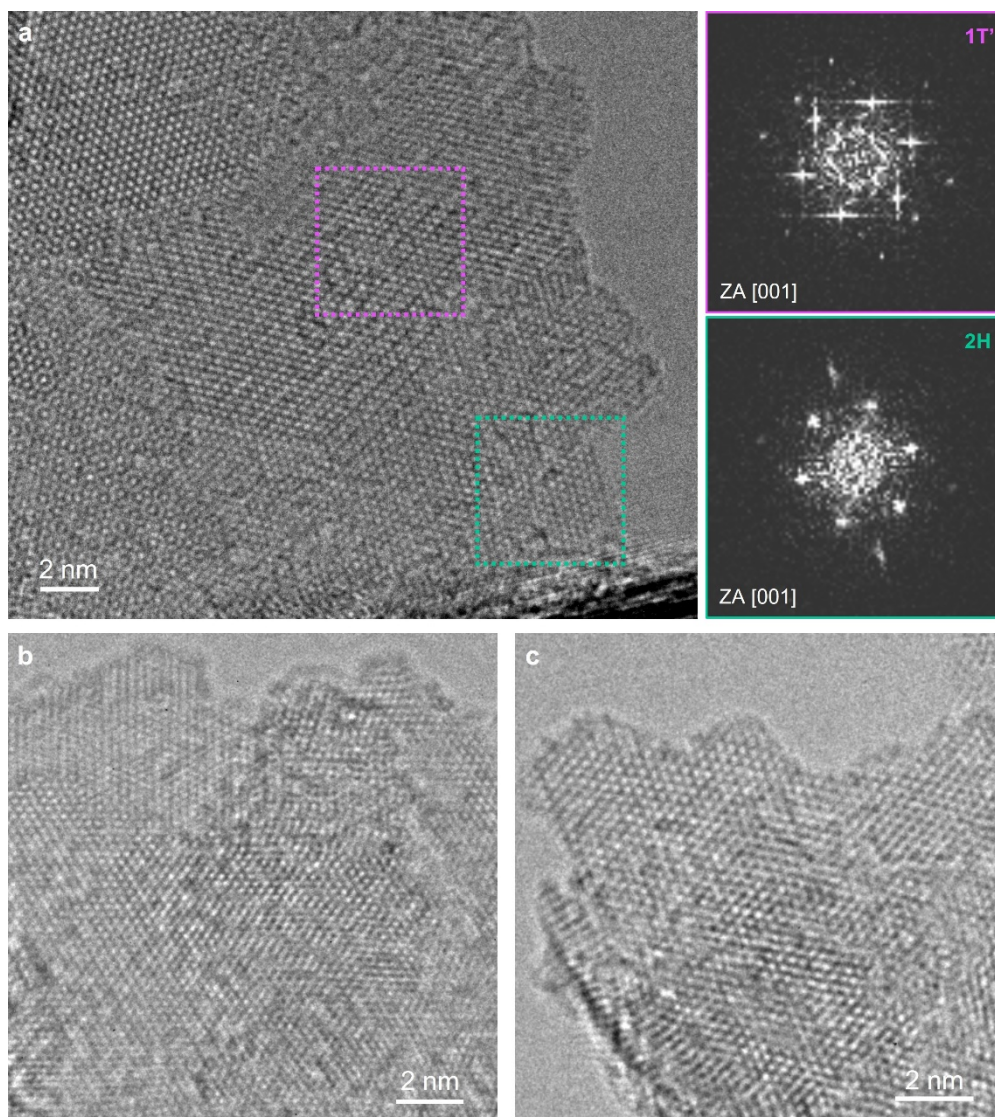
Supplementary Figure S7. The microstructure of $W_xMo_{1-x}Se_2$ nanoflowers. (a) High resolution TEM images of polycrystalline petals of $W_xMo_{1-x}Se_2$ $x = 0.50$ sample, demonstrating the co-existence of both the 1T' (purple box) and 2H (teal box) crystal phase domains. The respective FFT patterns are presented. (b, c) HR TEM image of W-rich ($x = 0.75$) and Mo-rich ($x = 0.25$) $W_xMo_{1-x}Se_2$ nanoflowers, respectively. The co-existing 1T'/2H crystal phases are seen in W-rich sample (panel b), and only the 2H crystal phase is seen in Mo-rich sample (panel c).
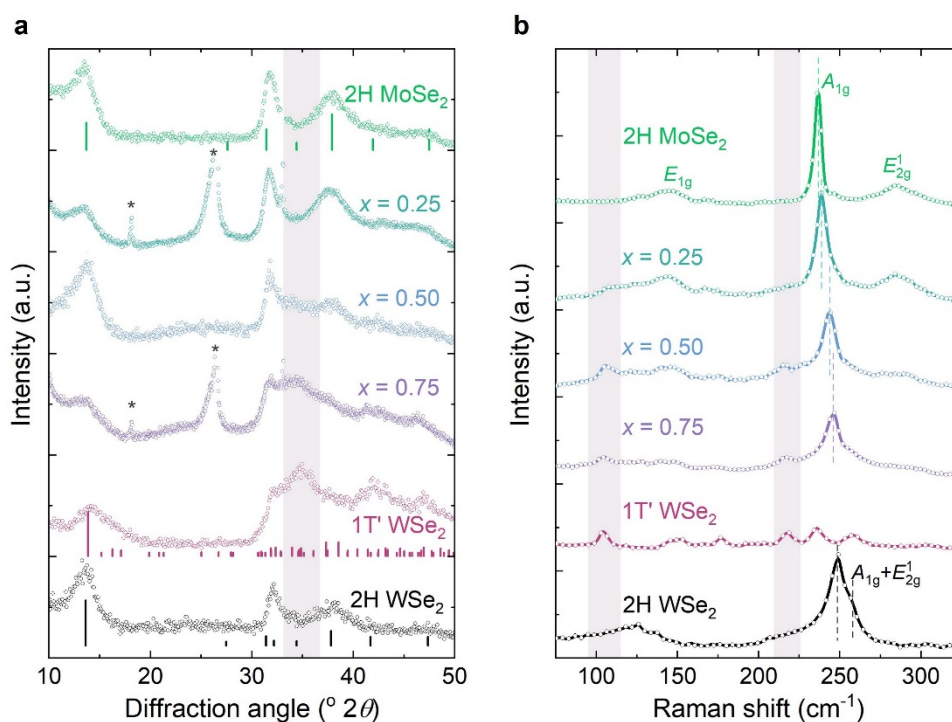
Supplementary Figure S8. XRD and Raman characterisation of the $W_xMo_{1-x}Se_2$ solid solutions. The representative diffractograms (panel a) and Raman spectra (panel b) of the $W_xMo_{1-x}Se_2$ nanosheets with $x = 0.75$; 0.50; and 0.25 grown directly on carbon paper are compared to the parent 2H $MoSe_2$ ($x = 0$), the as synthesised 1T' WSe_2 ($x = 1$), and the annealed 2H WSe_2 ($x = 1$) nanoflowers. The diffractograms (panel a) and Raman spectra (panel b) are offset for clarity.

In panel a, the standard diffraction patterns of bulk 2H $MoSe_2$ (green lines, ICDD 29-914) and 2H WSe_2 (black lines, ICDD 38-1388) are inserted for reference. The reference pattern of the 1T' WSe_2 (purple lines) was simulated based on the experimental lattice parameters from [6,7]. The diffraction peaks at 18.1 and 26.3 º2θ in the experimental diffractograms of the samples $x = 0.25$ and $x = 0.75$ (marked with asterisks) are assigned to the graphitic carbon residues present in XRD samples. In $W_xMo_{1-x}Se_2$ $x = 0.25$ and $x = 0.50$, three pronounced reflections centred at ~13.6, 31.8, and 37.8 º2θ match well the (002), (100) and (103) planes of the hexagonal 2H phase of either bulk $MoSe_2$ or WSe_2. A broad feature observed at ~34.8 º2θ in $W_xMo_{1-x}Se_2$ $x = 0.75$ resembles the prominent reflection of the $(\bar{1}12)$ planes of the monoclinic 1T' phase. This reflection is seen in the diffractograms of the as produced 1T' WSe_2 nanoflowers and is absent in the case of their thermally treated 2H counterpart. The peak broadening, caused by the polycrystallinity of colloidal $W_xMo_{1-x}Se_2$ solid solutions, renders the accurate phase analysis impossible. However, it should be noted that the gradual disappearance of this broad band with x decreasing illustrates the changing ratio of the coexisting crystal phases.

In panel b, the grey shaded boxes highlight the characteristic J_1 and J_3 modes used to track the 1T' component in $W_xMo_{1-x}Se_2$ solid solutions. Experimental Raman spectra of 1T' WSe_2 display six well-resolved Raman active modes at ~105-106, 145-149, 177, 218, 236, and 258-259 cm^{-1} [6,8]. Likewise, additional Raman active modes are present in Raman spectra of 1T' $MoSe_2$; these modes are centred at ~106-114 (J_1), 125-150 (J_2,), and 198-228 (J_3) [9–11] and are indicative of the existence of superlattice in the 1T' (distorted 1T) phase [12].
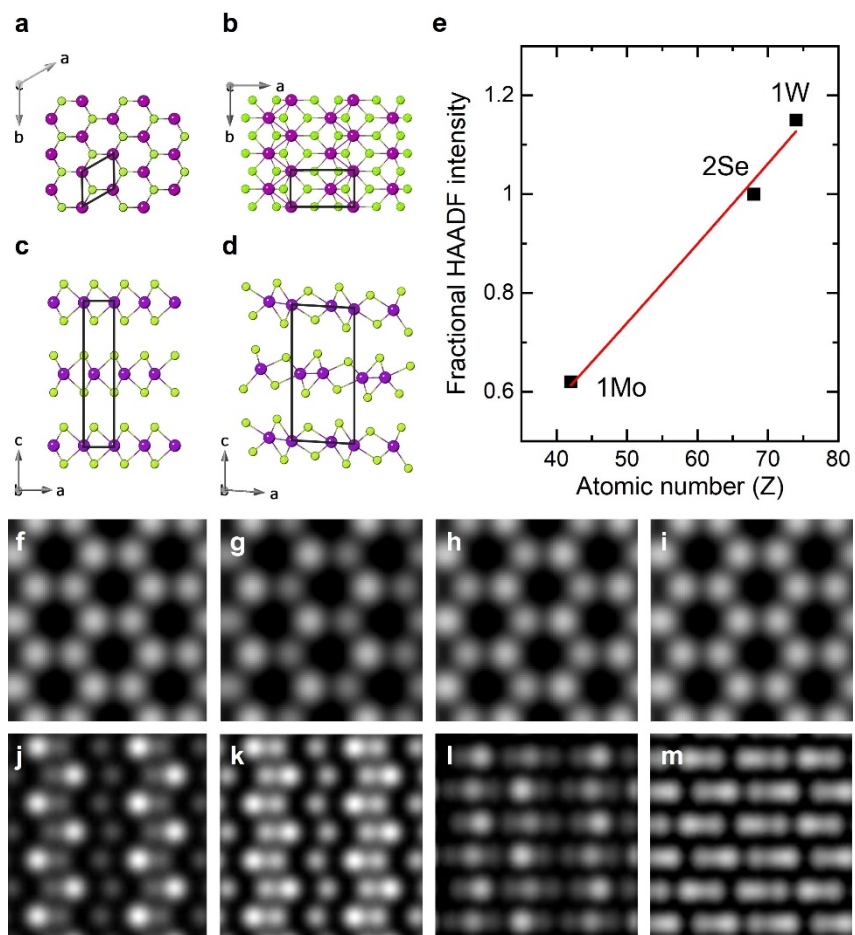
Supplementary Figure S9. Ball-and-stick models of the 2H (panels a and c) and 1T' (panels b and d) crystal phases. Simulated fractional HAADF signal intensities of the 1W, 1Mo, 2Se atomic sites (panel e). Simulated HAADF images of the 2H WSe$_2$ (panels f and h), 2H MoSe$_2$ (panels g and i), 1T' WSe$_2$ (panels j and l), and 1T' MoSe$_2$ (panels k and m) mono- and bilayers, respectively, used for initial, visual interpretation of STEM images.
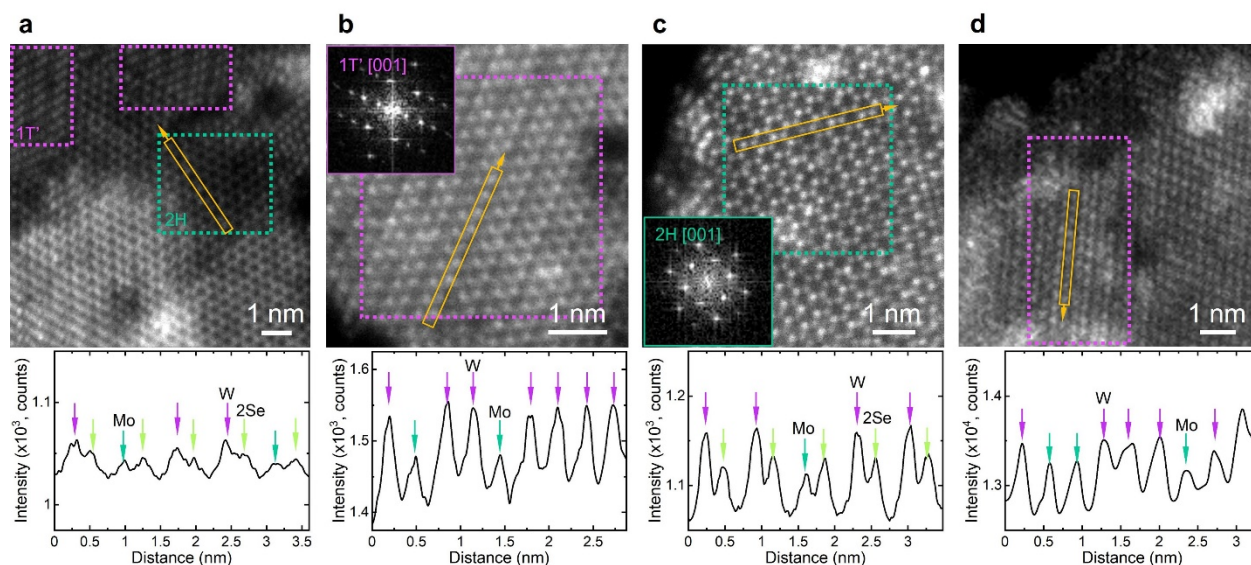
Supplementary Figure S10. Atomically resolved HAADF STEM images of the representative 2H (panels a and c) and 1T' (panels b and d) crystal phase domains in $W_xMo_{1-x}Se_2$ $x = 0.75$ (panels a and b) and $x = 0.50$ (panels c and d) samples. The intensity profiles along the cation-anion dumbbell lines in the 2H domains (panels a and c) and the cation lines in the 1T' domains (panels b and d) support the cation intermixing in both crystal phases of $W_{0.75}Mo_{0.25}Se_2$ (panels a and b) and $W_{0.50}Mo_{0.50}Se_2$ (panels b and d) monolayers. The corresponding lines of interest are highlighted by yellow boxes in the respective HAADF STEM images.
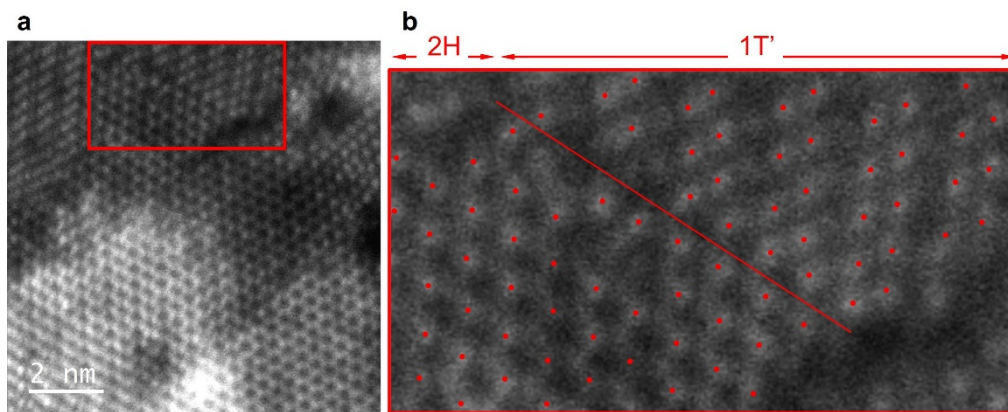
Supplementary Figure S11. Atomically resolved HAADF STEM scan (panel a) and a zoomed in area in the red box (panel b), illustrating the 1T'/2H interface as seen in a monolayer region in $W_xMo_{1-x}Se_2$ $x = 0.75$ sample. Red dots in the overlayed pattern in panel b represent the identified transition metal sites.
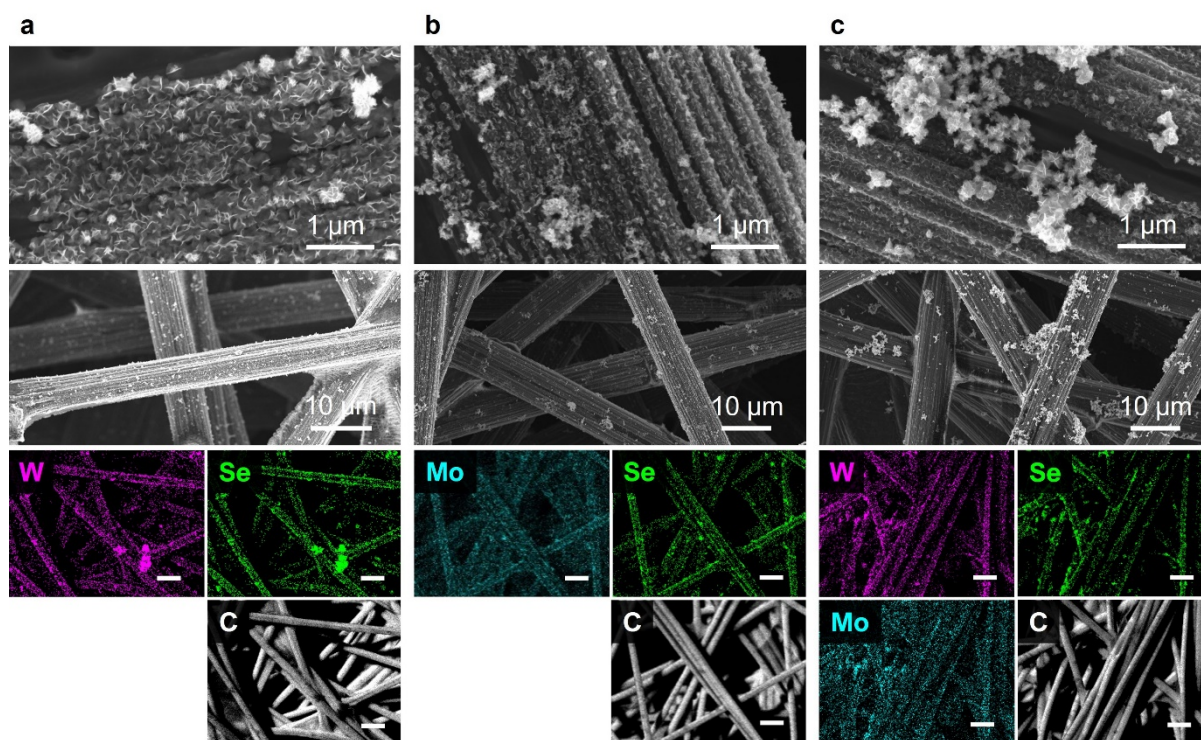
Supplementary Figure S12. Growth of $W_xMo_{1-x}Se_2$ nanosheets directly on functional supports. The zoomed in (top row) and overview SEM images (middle row), and the representative EDS elemental maps (bottom row; scale bar 20 µm) of the WSe_2 (panel a), $MoSe_2$ (panel b), and $W_xMo_{1-x}Se_2$ $x = 0.50$ (panel c) vertical nanosheets grown directly on carbon paper for the electrochemical testing.
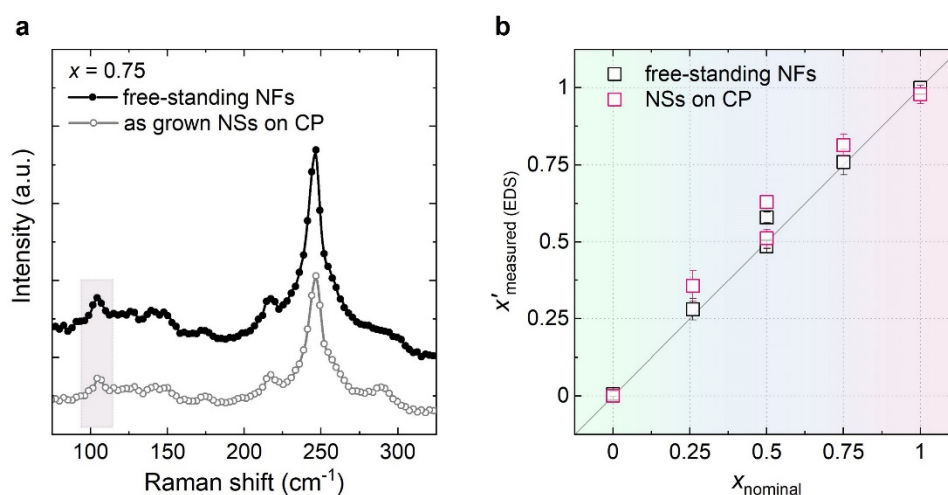
Supplementary Figure S13. Physical characterisation of binary $W_xMo_{1-x}Se_2$ nanosheets on CP (NSs@CP) and free-standing $W_xMo_{1-x}Se_2$ nanoflowers (fs NFs) formed as a side-product. The representative Raman spectra of free-standing $W_xMo_{1-x}Se_2$ nanoflowers (NFs) and nanosheets (NSs) anchored on carbon paper ($x = 0.75$) that demonstrate the resulting crystal phase was not affected by the heterogeneous nucleation (panel a). The correlation between the nominal composition x and the measured composition x' of binary $W_xMo_{1-x}Se_2$ NSs@CP and the corresponding free-standing $W_xMo_{1-x}Se_2$ NFs grown from TM P + Se SS (panel b).

Table S3. Physical characterisation of binary $W_xMo_{1-x}Se_2$ nanosheets on CP (NSs@CP) and free-standing $W_xMo_{1-x}Se_2$ nanoflowers (fs NFs) formed as a side-product. The $W_xMo_{1-x}Se_2$ nanosheets on CP were then tested as working electrodes for the HER without any post-growth treatment. x is the nominal chemical composition, x' is the measured chemical composition (from EDS, XPS and XRF data); 1T' (at.%) is the total metastable crystal phase content determined from the XPS data.

| Material | x | x' | | | | 1T', (at.%) |
		fs NFs /EDS/	NSs@CP /EDS/	NSs@CP /XPS/	NSs@CP /XRF/	/XPS/
WSe_2	1	1	0.98±0.03	1	1	49
$W_{0.75}Mo_{0.25}Se_2$	0.75	0.76±0.04	0.81±0.03	0.7	0.85	44
$W_{0.50}Mo_{0.50}Se_2$	0.50	0.58±0.02	0.63±0.02	0.52	0.67	13
$W_{0.25}Mo_{0.75}Se_2$	0.25	0.28±0.03	0.36±0.05	0.32	0.44	6
$MoSe_2$	0	0.01±0.01	0	0	0.03	0

Table S4. HER performance of $W_xMo_{1-x}Se_2$ on CP working electrodes as presented in Figure 4.e. x is the nominal chemical composition, x' is the measured chemical composition, v is the amount of active material (in $\mu mol/cm^2$) and m is the respective mass loading (in $\mu g/cm^2$), η_{-10} is the overpotential (in mV) required to reach the benchmarking current density of -10 mA/cm^2, η_{-20} is the overpotential (in mV) required to reach the current density of -20 mA/mg, b is the Tafel slope (in mV/dec).

Material	x	x'	v, ($\mu mol/cm^2$) /ICP AES/	Mass loading m, ($\mu g/cm^2$) /ICP AES/	η_{-10}, (mV)	η_{-20}, (mV)	b (mV/dec)
WSe_2	1	0.98	1.312	448.2	556	551	152
$W_{0.75}Mo_{0.25}Se_2$	0.75	0.81	0.925	300.5	466	435	143
$W_{0.50}Mo_{0.50}Se_2$	0.50	0.63	0.955	295.3	420	381	155
$W_{0.25}Mo_{0.75}Se_2$	0.25	0.36	0.596	170.0	436	357	169
$MoSe_2$	0	0	0.437	111.0	291	195	137

Table S5. Comparison with the reported nanostructured $MoSe_2$ and WSe_2 catalysts as presented in Figure 4.f. *m* is the active material mass loading per working electrode (in mg/cm²), η_{-10} is the overpotential (in mV), at which the working electrode reaches the benchmarking current density of -10 mA/cm², *b* is the Tafel slope (in mV/dec).

Material	Mass loading *m*, (mg/cm²)	Overpotential η_{-10}, (mV)	Tafel slope *b* (mV/dec)	Reference
$MoSe_2$ (HTS, 2H)	0.140	355	146	[13]
$MoSe_2$ (CS, 2H)	0.285	280	98	[14]
$MoSe_2$ (CS, 2H)	0.111	291	137	This work
WSe_2 (CS, 2H)	0.400	453	250	[15]
WSe_2 (CS, 2H)	1	372	105	[16]
WSe_2 (CS, 1T'/2H)	0.448	556	152	This work
Mn:$MoSe_2$ (CS, 2.4 at.%, 2H)	0.530	167	60	[17]
$V_xMo_{1-x}Se_2$ (CS, 1T/2H)	0.390	114	43	[18]
$Nb_xMo_{1-x}Se_2$ (CS, 1T/2H)	0.390	140	46	[19]
Ni:WSe_2 (CS, 3 at.%, 2H)	1	278	81	[16]
Nb:WSe_2 (CS, 3 at.%, 2H)	1	300	95	[16]
Nb:WSe_2 (PVT+LPE, 1T/2H)	0.057	750	124	[20]
$W_xMo_{1-x}Se_2$ (CS, *x'*=0.63, 1T'/2H)	0.295	420	155	This work
$W_xMo_{1-x}Se_2$ (CS, x=0.43, 2H)	1	209	76	[21]

Table S6. The 1T'-to-2H transition temperature T.

Material	T, °C	Reference
$MoSe_2$	125	[8]
WSe_2	390	[6]

References

1   G. G. Yordanov, H. Yoshimura and C. D. Dushkin, *Colloid Polym Sci*, 2008, **286**, 813–817.

2   Z. Deng, L. Cao, F. Tang and B. Zou, *J Phys Chem B*, 2005, **109**, 16671–16675.

3   L. C. Frenette and T. D. Krauss, *Nat Commun*, 2017, **8**, 2082.

4   T. P. A. Ruberu, H. R. Albright, B. Callis, B. Ward, J. Cisneros, H. Fan and J. Vela, *ACS Nano*, 2012, **6**, 5348–5359.

5   S. K. Srivastava and B. N. Avasthi, *J Mater Sci*, 1985, **20**, 3801–3815.

6   M. S. Sokolikova, P. C. Sherrell, P. Palczynski, V. L. Bemmer and C. Mattevi, *Nat Commun*, 2019, **10**, 712.

7   J. Q. Geisenhoff, A. K. Tamura and A. M. Schimpf, *Chemical Communications*, 2019, **55**, 8856–8859.

8   Z. Lai, Q. He, T. H. Tran, D. V. M. Repaka, D.-D. Zhou, Y. Sun, S. Xi, Y. Li, A. Chaturvedi, C. Tan, B. Chen, G.-H. Nam, B. Li, C. Ling, W. Zhai, Z. Shi, D. Hu, V. Sharma, Z. Hu, Y. Chen, Z. Zhang, Y. Yu, X. Renshaw Wang, R. v. Ramanujan, Y. Ma, K. Hippalgaonkar and H. Zhang, *Nat Mater*, 2021, **20**, 1113–1120.

9   I. S. Kwon, I. H. Kwak, T. T. Debela, H. G. Abbas, Y. C. Park, J. Ahn, J. Park and H. S. Kang, *ACS Nano*, 2020, **14**, 6295–6304.

10   M. Naz, T. Hallam, N. C. Berner, N. McEvoy, R. Gatensby, J. B. McManus, Z. Akhter and G. S. Duesberg, *ACS Appl Mater Interfaces*, 2016, **8**, 31442–31448.

11   U. Gupta, B. S. Naidu, U. Maitra, A. Singh, S. N. Shirodkar, U. v. Waghmare and C. N. R. Rao, *APL Mater*, 2014, **2**, 092802.

12   S. Jiménez Sandoval, D. Yang, R. F. Frindt and J. C. Irwin, *Phys Rev B*, 1991, **44**, 3955–3962.

13   Y. Yin, Y. Zhang, T. Gao, T. Yao, X. Zhang, J. Han, X. Wang, Z. Zhang, P. Xu, P. Zhang, X. Cao, B. Song and S. Jin, *Advanced Materials*, 2017, **29**, 1700311.

14   X. Zhou, J. Jiang, T. Ding, J. Zhang, B. Pan, J. Zuo and Q. Yang, *Nanoscale*, 2014, **6**, 11046–11051.

15   M. Muska, J. Yang, Y. Sun, J. Wang, Y. Wang and Q. Yang, *ACS Appl Nano Mater*, 2021, **4**, 5796–5807.

16   S. R. Kadam, A. N. Enyashin, L. Houben, R. Bar-Ziv and M. Bar-Sadan, *J Mater Chem A Mater*, 2020, **8**, 1403–1416.

17   V. Kuraganti, A. Jain, R. Bar-Ziv, A. Ramasubramaniam and M. Bar-Sadan, *ACS Appl Mater Interfaces*, 2019, **11**, 25155–25162.

18   I. S. Kwon, I. H. Kwak, T. T. Debela, J. Y. Kim, S. J. Yoo, J.-G. Kim, J. Park and H. S. Kang, *ACS Nano*, 2021, **15**, 14672–14682.

19   I. S. Kwon, I. H. Kwak, J. Y. Kim, T. T. Debela, Y. C. Park, J. Park and H. S. Kang, *ACS Nano*, 2021, **15**, 5467–5477.

20   X. Chia, N. A. A. Sutrisnoh, Z. Sofer, J. Luxa and M. Pumera, *Chemistry - A European Journal*, 2018, **24**, 3199–3208.

21   O. E. Meiron, V. Kuraganti, I. Hod, R. Bar-Ziv and M. Bar-Sadan, *Nanoscale*, 2017, **9**, 13998–14005.